ACS APPLIED MATERIALS & INTERFACES

www.acsami.org Research Article

Design and Radiation-Responsive Applications of Hafnium-Organic Frameworks Based on Aggregation-Induced Emission

Yong Chen, Zhiheng Xu,* Tiancheng Xu, Zhiyi Xu, Xuebin Zhang, Yuqiao Wang, and Xiaobin Tang*

Cite This: *ACS Appl. Mater. Interfaces* 2025, 17, 47553−47561 Read Online

ACCESS | Metrics & More | Article Recommendations | Supporting Information

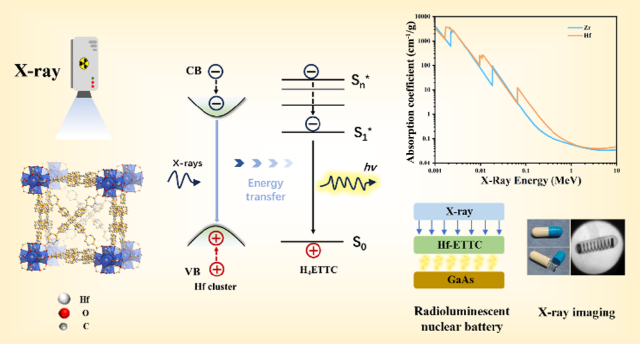

ABSTRACT: The development of functional materials capable of converting high-energy radiation into visible light is crucial for advancing technologies in radiation energy conversion and imaging detection. In this study, a highly luminescent metal−organic framework (Hf-ETTC) was successfully synthesized via a mild solvothermal method utilizing the directed self-assembly of aggregation-induced emission (AIE)-active ligands with hafnium-oxo clusters. The high atomic number of the hafnium centers significantly enhanced the energy absorption efficiency, effectively promoting the radioluminescent behavior of the AIE-active ligands and resulting in an exceptional PLQY of 90.72%. Experimental results revealed that Hf-ETTC embedded in a PDMS matrix exhibited strong luminescence under X-ray excitation and demonstrated sensitivity to radiation dose rates as low as 1.1 μGy s^{-1}. The radioluminescent performance of Hf-ETTC@PDMS was further validated through the fabrication of a radioluminescent nuclear battery and an X-ray imaging system. The nuclear battery achieved a maximum output power density of 0.19 μW cm^{-2} at a dose rate of 5.6 μGy s^{-1}. Additionally, flexible X-ray imaging with a spatial resolution of 402 μm was successfully achieved. This work highlights a synergistic strategy combining high-Z Hf elements with the AIE effect, offering valuable insights for the structural design, optical enhancement, and radiation-responsive applications of luminescent metal−organic frameworks.

KEYWORDS: *hafnium metal cluster, aggregation-induced emission, energy conversion, radioluminescent nuclear battery, X-ray imaging*

1. INTRODUCTION

Scintillators are a class of luminescent materials that respond to high-energy radiation by converting ionizing radiation into visible light.[1−4] They have attracted significant attention in applications such as medical imaging[5−7] and radiation monitoring.[8,9] High-performance scintillators typically integrate strong radiation-stopping power with efficient luminescent centers. Heavy metals with high atomic numbers (Z) enhance X-ray attenuation, while organic ligands offer advantages in processability, structural tunability, and rapid response times compared with their inorganic counterparts.

Metal−organic frameworks (MOFs) exhibit exceptional promise as scintillators due to their unique structural features, which facilitate synergistic interactions between metal nodes and luminescent ligands.[10,11] Compared to conventional inorganic scintillators (e.g., CsI:Tl, $Bi_4Ge_3O_{12}$), MOF-based scintillators offer three key advantages: (1) Their modular architecture allows atomic-level precision in tuning both metal centers and organic ligands, enabling the synergistic optimization of X-ray absorption efficiency and luminescence performance. (2) The porous framework effectively suppresses self-absorption and exciton quenching effects. (3) Enhanced radiation stability improves material durability under prolonged exposure.[12] Among MOF scintillators, zirconium (Zr, Z = 40)-based systems (e.g., UiO-66 and NU-1000) have become research priorities due to their excellent chemical stability and moderate X-ray attenuation capabilities.[13−16] However, the X-ray absorption efficiency of Zr-based MOFs declines significantly when radiation energy exceeds a critical threshold, severely limiting their applicability in deep-tissue imaging and high-energy radiation conversion.[17−19]

Heavy metal elements are highly efficient at absorbing radiation energy.[20−22] In this study, we propose a synergistic strategy that combines the ″high-Z element″ approach with ″aggregation-induced emission (AIE) enhancement″. Hafnium (Hf), a high-Z element from the same main group as Zr, was selected as the metal node. The organic ligand H_4ETTC, a derivative of tetraphenylenylene (TPE), was chosen for its AIE-active properties.[23−26] The strong X-ray absorption

Received: June 30, 2025
Revised: August 5, 2025
Accepted: August 5, 2025
Published: August 11, 2025

capability of Hf, combined with efficient directional energy transfer,[27] significantly enhances the radioluminescence performance of the AIE-active materials. To further broaden the application potential, MOF-polymer composites were developed, enabling them to be used as flexible scintillators.

Hf-ETTC crystals were successfully synthesized via a solvothermal method. The material exhibited an exceptional photoluminescence quantum yield (PLQY) of 90.72%, significantly surpassing that of the pristine H_4ETTC ligand (47.61%) and the isostructural Zr-based MOF PCN-94 (75%)[28] under ambient conditions. Additionally, the robust framework structure of Hf-ETTC, reinforced by ultrastrong Hf−O coordination bonds, confers excellent stability under high-dose irradiation as well as extreme temperature and humidity conditions. To extend its applicability, Hf-ETTC was incorporated into a polydimethylsiloxane (PDMS) matrix to fabricate flexible composite films. Under X-ray excitation, the resulting Hf-ETTC@PDMS composites exhibited strong radioluminescence (RL) with a detection limit as low as 1.1 μGy s^{-1}. Notably, owing to the high atomic number of Hf, the enhancement of radioluminescence performance at high dose rates is substantially more pronounced compared to that of zirconium. Furthermore, the exceptional performance of Hf-ETTC@PDMS in both radioluminescent nuclear battery and X-ray imaging applications validates the synergistic advantage of combining high-Z elements with AIE-active ligands. This study not only establishes a new paradigm for the design of MOF-based scintillators but also provides a theoretical and technical foundation for developing next-generation, high-performance scintillators through the integration of high-Z elements and AIE strategies.

2. RESULTS AND DISCUSSION

2.1. Characterization of the As-Synthesized Hf-ETTC.

Hf-ETTC was synthesized by a solvothermal method. As shown in Figure 1a, under the mediation of acetic acid, Hf^{4+} ions initially formed Hf_6O_8 metal cluster nodes, which subsequently coordinated with the AIE-active H_4ETTC ligands (Figure 1b). This coordination resulted in the construction of a novel metal−organic framework with a cubic cage-type. In this architecture, Hf_6O_8 clusters serve as the vertices, each bridged by 12 ETTC ligands to 18 neighboring metal clusters, forming a three-dimensional framework with an edge length of approximately 21.104 Å (Figure 1c).

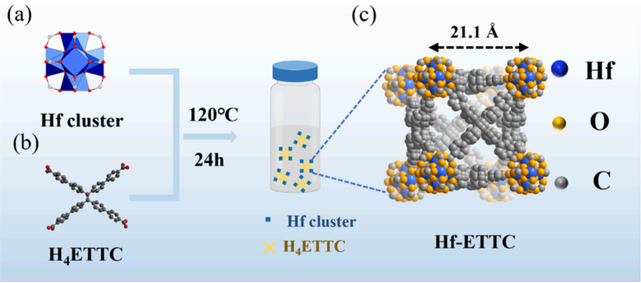

Figure 1. (a) Preassembled Hf-oxo clusters derived from $HfCl_4$. (b) Molecular structure of organic ligand H_4ETTC. (c) Stacking model illustrating the crystalline packing arrangement.

Structural characterization revealed excellent consistency between the experimental powder X-ray diffraction (PXRD) patterns and the simulated data, confirming the phase purity and structural integrity (Figure 2a). The nitrogen adsorption isotherms obtained at 77 K revealed the pore characteristics of Hf-ETTC, including a BET specific surface area of 1566 $m^2 \cdot g^{-1}$ and an average pore size of 2.05 nm, which aligns with the corresponding crystal structure (as illustrated in Figure 2b). Scanning electron microscopy (SEM) images at various magnifications (Figure 2c) displayed well-defined cubic crystals, which were in good agreement with the theoretically predicted morphology. Energy-dispersive X-ray spectroscopy (EDS) analysis confirmed the expected stoichiometric ratios of Hf, C, and O (Figures S1 and S2), validating the elemental composition. Thermogravimetric analysis (TGA) revealed that the mass loss observed below 520 °C was due to the desorption of guest molecules, while the MOF framework itself remained thermally stable, highlighting its exceptional thermal robustness (Figure S3). Fourier transform infrared spectroscopy (FTIR) analysis indicated that the stretching vibration of C=O at 1692.3 cm^{-1} disappeared compared with the H_4ETTC ligand, providing evidence for the formation of coordination bonds between the H_4ETTC ligand and Hf^{4+} (Figure S4).

2.2. Optical Properties of Hf-ETTC.

The UV−vis absorption spectra (Figure 3a) showed that Hf-ETTC retained the absorption peaks at 350−500 nm similar to those of the H_4ETTC ligands but exhibited significantly enhanced absorption intensity. The redshift observed in the UV−vis spectrum following the formation of the MOF structure is primarily attributed to orbital hybridization between the metal nodes and the organic ligands. This interaction lowers the electronic transition energy. Moreover, the intrinsic rigidity of the MOF framework promotes ligand planarization and $\pi-\pi$ stacking interactions, thereby extending the conjugated system. All of these will lead to a redshift of the absorption peak.[29,30] Photoluminescence (PL) measurements under the optimal excitation conditions showed yellow emission at 530 nm for both the free ligand and the Hf-ETTC framework. Variations in excitation wavelength led to differing excitation efficiencies of the luminescent centers and energy transfer efficiencies between frames, consequently resulting in distinct emission colors under different excitation conditions. (As shown in the spectrum and the illustration in Figure 3b, the specific PL spectra are shown in Figure S5.) However, the framework displayed markedly stronger emission and excitation spectra, as shown in Figure 3b. This luminescence enhancement is consistent with that observed in the isostructural Zr-based MOF, PCN-94, confirming that metal cluster nodes facilitate radiative recombination in AIE-active ligands.

Quantitative analysis revealed a PLQY of 90.72% for Hf-ETTC (Figure S6), nearly twice that of the free H_4ETTC ligands (47.61%). This enhancement is consistent with the general nonradiative decay pathways in H_4ETTC, such as torsional relaxation, that were suppressed within the solid framework, leading to enhanced luminescence. Fluorescence lifetime measurements further revealed that Hf-ETTC exhibited an excited-state fluorescence lifetime of 4.1 ns, compared to 3.4 ns for the organic ligands (Figure 3c). Additionally, the optical attenuation lifetime of Hf-ETTC is comparable to those of commercial scintillators, indicating its potential as a high-performance scintillating material.

Building on the superior photophysical properties of Hf-ETTC, including its high PLQY and short excited-state lifetime, we systematically evaluated its RL performance. As shown in Figure 3d, the RL intensity exhibited a clear dose rate-dependent enhancement, demonstrating a proportional relationship with increasing radiation levels. As shown in

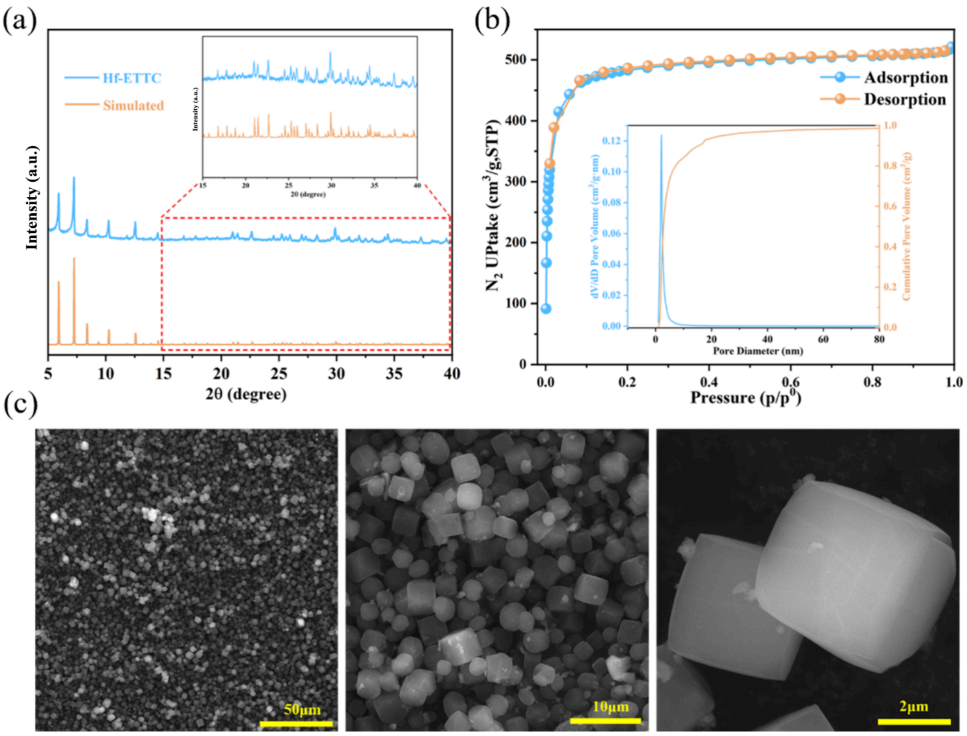

Figure 2. (a) PXRD patterns of Hf-ETTC. Inset: detailed drawing within the range of 15−40°. (b) N_2 adsorption−desorption isotherm of Hf-ETTC measured at 77 K. Inset: pore size distribution. (c) SEM images of Hf-ETTC at various magnifications.

Figure 3e, the RL spectrum displayed yellow emission, consistent with the PL spectrum, suggesting that the emitted photons originate from the radiative recombination of singlet excitons in the AIE-active organic ligands within the MOF. Notably, the synergistic interaction between the Hf metal clusters and the AIE-active ligands resulted in a 5-fold enhancement in RL intensity compared to the free ligand and significantly outperformed the isostructural Zr-based MOF (PCN-94), primarily because the Hf element exhibits a higher X-ray absorption capacity compared to the Zr element (Figure S7). Furthermore, as shown in Figure 3f, the RL intensity of Hf-ETTC progressively surpassed that of PCN-94 (Zr-ETTC) with rising dose rates, further highlighting the critical role of the high-*Z* Hf centers in boosting luminescence performance within the MOF architecture. A similar enhancement mechanism was observed under X-ray excitation, as illustrated in Figure 3g. Initially, X-ray photons interact with the Hf clusters, ejecting inner-shell electrons through photoelectric absorption. This is followed by electron−electron scattering and Auger processes, generating numerous secondary electrons and electron−hole pairs. The ETTC ligands are subsequently excited through energy transfer from electron−hole recombination, resulting in intrinsic radioluminescence emission under X-ray irradiation.[31]

2.3. Luminescence Stability of Hf-ETTC.

Environmental stability tests revealed the exceptional durability of the Hf-ETTC material. Temperature-dependent PL studies conducted over the range of 73−473 K yielded an exciton binding energy (ΔE) of 201.6 meV, calculated through Arrhenius equation fitting, as shown in Figure 4a. The corresponding PL spectra at various temperatures are presented in Figure S8. The relatively high ΔE value effectively suppresses the nonradiative recombination pathways, thereby ensuring stable luminescence performance across a wide temperature range. The temperature-dependent PL intensity data were fitted using the Arrhenius equation:[32]

$$\frac{I(T)}{I_0} = \frac{1}{I + A\exp(-\frac{\Delta E}{k_B T})} \tag{1}$$

where I_0 is the PL intensity at 273 K temperature, A represents the frequency factor, which is a constant, and k_B represents the Boltzmann constant.

Furthermore, Hf-ETTC retained 82% of its initial RL intensity after 60 days of immersion in deionized water, demonstrating excellent moisture resistance (Figure 4b). Detailed spectral data supporting this observation are presented in Figure S9. As shown in Figure S10, after soaking in water for 60 days, the diffraction peaks and intensity of its PXRD pattern did not change significantly, indicating its structural stability in water. Long-term equivalent irradiation experiments further confirmed the structural robustness of the material. PXRD analysis showed no signs of framework degradation following cumulative radiation exposure, highlighting the material's outstanding radiation hardness (Figure 4c). Even after a total absorbed dose of 5980 Gy, Hf-ETTC maintained 78% of its original RL output (Figure 4d). The RL spectrum after irradiation is shown in Figure S11. The strong metal−ligand coordination bond (Hf−O) enhances the stability of Hf-ETTC under conditions of high temperature, high humidity, and radiation.[13,33] Taken together, these characteristics demonstrate that Hf-ETTC integrates high luminescence efficiency with outstanding resistance to humidity, temperature extremes, and strong irradiation environment stability. These features establish a strong physical basis for its practical application in radioluminescent nuclear batteries and X-ray imaging under extreme environmental conditions.

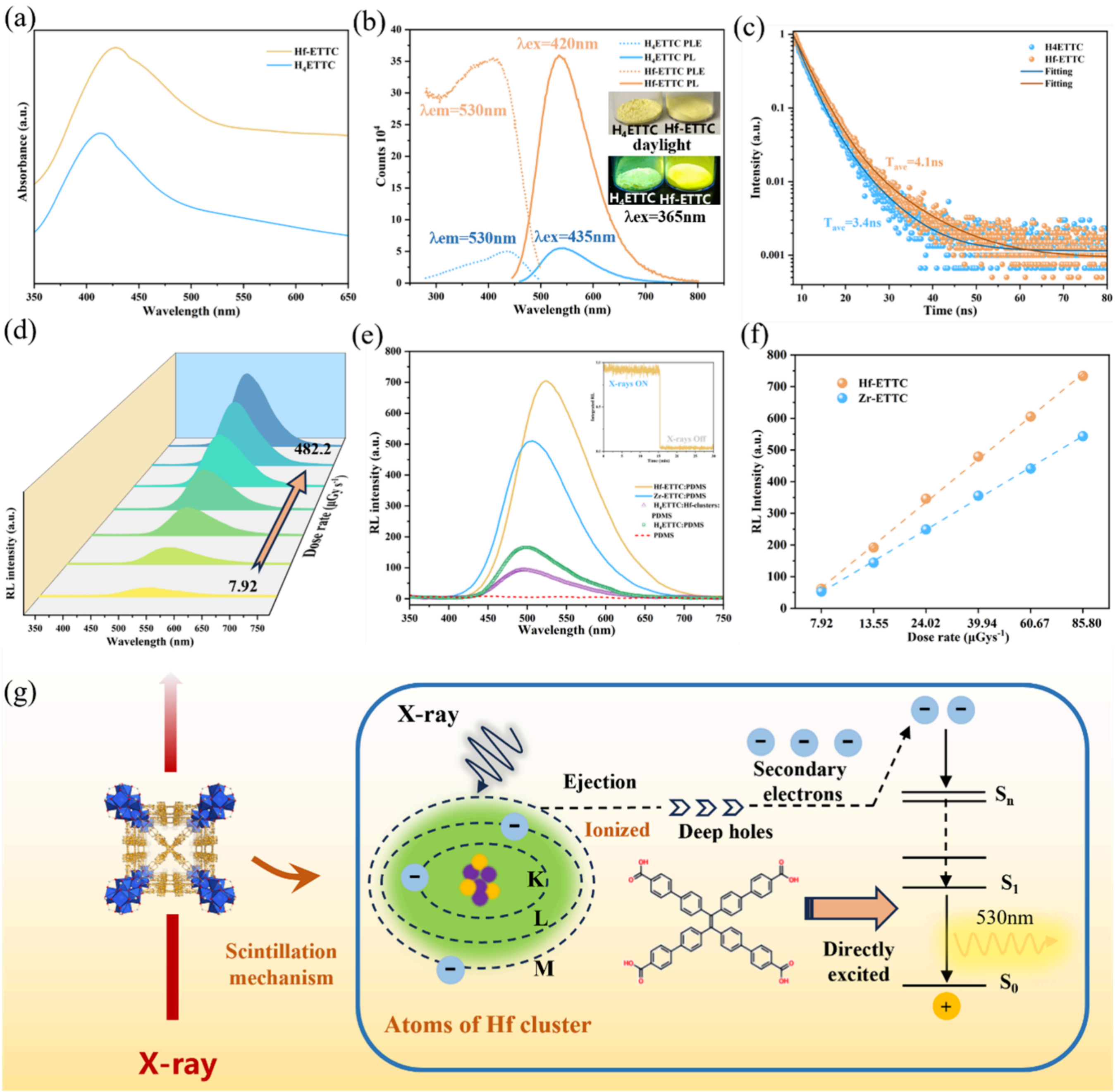

Figure 3. (a) UV−vis absorption spectra of H_4ETTC and Hf-ETTC. (b) PL emission and PLE spectra of H_4ETTC and Hf-ETTC. (c) Emission decay curves of H_4ETTC and Hf-ETTC monitored at 530 nm. (d) RL spectra of Hf-ETTC under varying X-ray dose rates (7.92−482.2 μGy s^{-1}). (e) Comparative RL spectra of PDMS-based composites: Hf-ETTC@PDMS, H_4ETTC@PDMS, PDMS containing separate Hf-oxo clusters and H_4ETTC ligands, and Zr-ETTC@PDMS. (f) Dose rate-dependent RL intensity comparison between Hf-ETTC and Zr-ETTC. (g) Schematic illustration of the proposed RL enhancement mechanism.

2.4. Application of Hf-ETTC@PDMS in the Radioluminescent Nuclear Battery.

To broaden its application potential, flexible Hf-ETTC@PDMS composite films were fabricated by using blade coating. Under X-ray excitation, the films exhibited intense yellow luminescence, attributed to the suppression of nonradiative transitions in the ligands by the MOF framework, as shown in Figure S12. It exhibits a high degree of flexibility and tensile resistance, as illustrated in Figure S13 and Table S1. This study investigated the use of Hf-ETTC@PDMS flexible films for X-ray absorption and energy conversion applications. The radioluminescent nuclear battery represents a key approach to X-ray energy conversion technology. As illustrated in Figure 5a, the operational mechanism involves three sequential processes: X-ray excitation of the scintillators to generate visible photons, absorption of this light by a photovoltaic device, and conversion into electrical energy.[34,35]

Fluorescent materials are critical in this energy conversion cascade, as their high luminescence efficiency and stability directly influence the overall performance of the radioluminescent nuclear battery. For a systematic evaluation, GaAs photovoltaic components with a spectral response well-matched to the emission band of Hf-ETTC were employed.

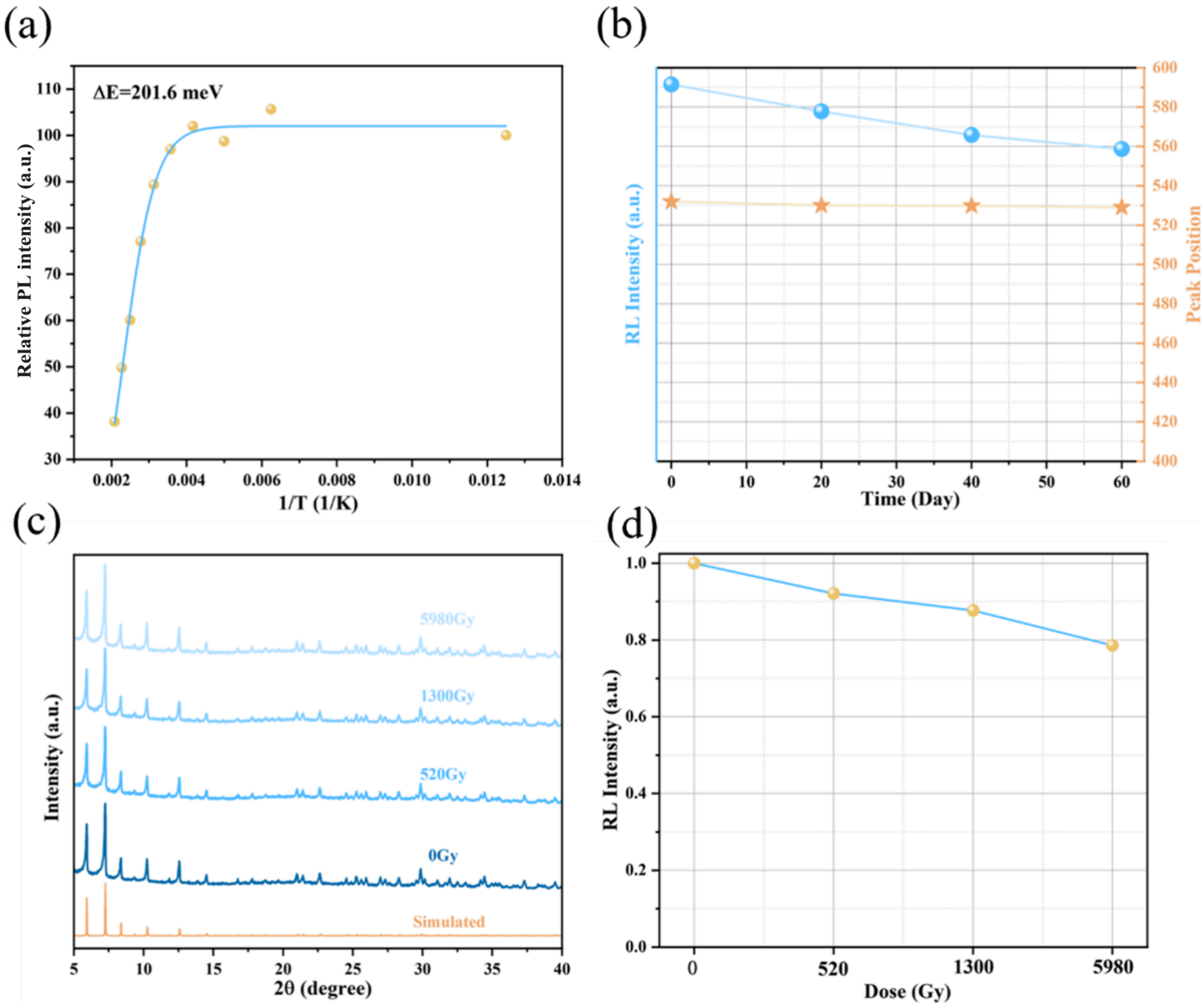

Figure 4. (a) Temperature-dependent PL intensity of Hf-ETTC plotted as a function of reciprocal temperature (73−473 K). (b) RL intensity and peak position shifts of Hf-ETTC after 60 days of immersion in deionized water. (c) PXRD patterns of Hf-ETTC after exposure to irradiation doses using an ^{60}Co source at a dose rate of 260 Gy·h^{-1}. (d) RL intensity attenuation profile of Hf-ETTC following exposure to various irradiation doses.

Figure 5b illustrates the experimental setup, and the EQE was calculated using the following formula:[36]

$$\mathrm{EQE} = \frac{I/q}{p/h\nu} \tag{2}$$

where I/q represents the number of photogenerated electron−hole pairs per unit time, I is the photocurrent, and q is the elementary charge. The term $p/h\nu$ denotes the number of incident photons on the photovoltaic module surface per unit time, where p is the incident light power and $h\nu$ is the energy of a single photon, allowing calculation of the photon flux in photons per second.

As shown in Figure 5c, the electrical output of the radioluminescent nuclear battery increased proportionally with radiation dose rate, with both output power and energy conversion efficiency showing progressive improvement. At a dose rate of 5.9 μGy s^{-1}, the device achieved a maximum output power density of 0.19 μW cm^{-2} (Figure 5d) and an energy conversion efficiency of 0.0583%, surpassing the previously reported benchmark of 0.023%;[37] this performance is comparable to those of other high-quality scintillators, as presented in Table S2. The equivalent X-ray power at this dose rate was approximately 1.305 mW, with the corresponding X-ray energy spectrum presented in Figure S14. Furthermore, when compared to a device utilizing CsPbBr$_3$ quantum dots as transducer materials, under an irradiation intensity of 4.2 μGy s^{-1} (X-ray tube settings: 25 kV and 1 mA), the maximum output power was 0.315 μW.[38] The Hf-ETTC@PDMS system demonstrated a higher output power of 0.514 μW under the same excitation conditions. These results validate the significant potential of the Hf-ETTC@PDMS composite for efficient radiation energy conversion technologies.

2.5. Application of Hf-ETTC@PDMS in X-ray Radiation Imaging.

This study further explored the potential of Hf-ETTC@PDMS composite films for X-ray imaging applications, as shown in Figure 6a. Leveraging the material's exceptional flexibility (Figure 6b), high luminescence performance, and environmental stability, we conducted dose−response analysis critical to X-ray imaging technologies. These rely on the dose-dependent intensity of RL to generate phase-contrast images. As shown in Figure 6c, the Hf-ETTC@PDMS exhibits a favorable dose responsiveness with an X-ray response thresh-

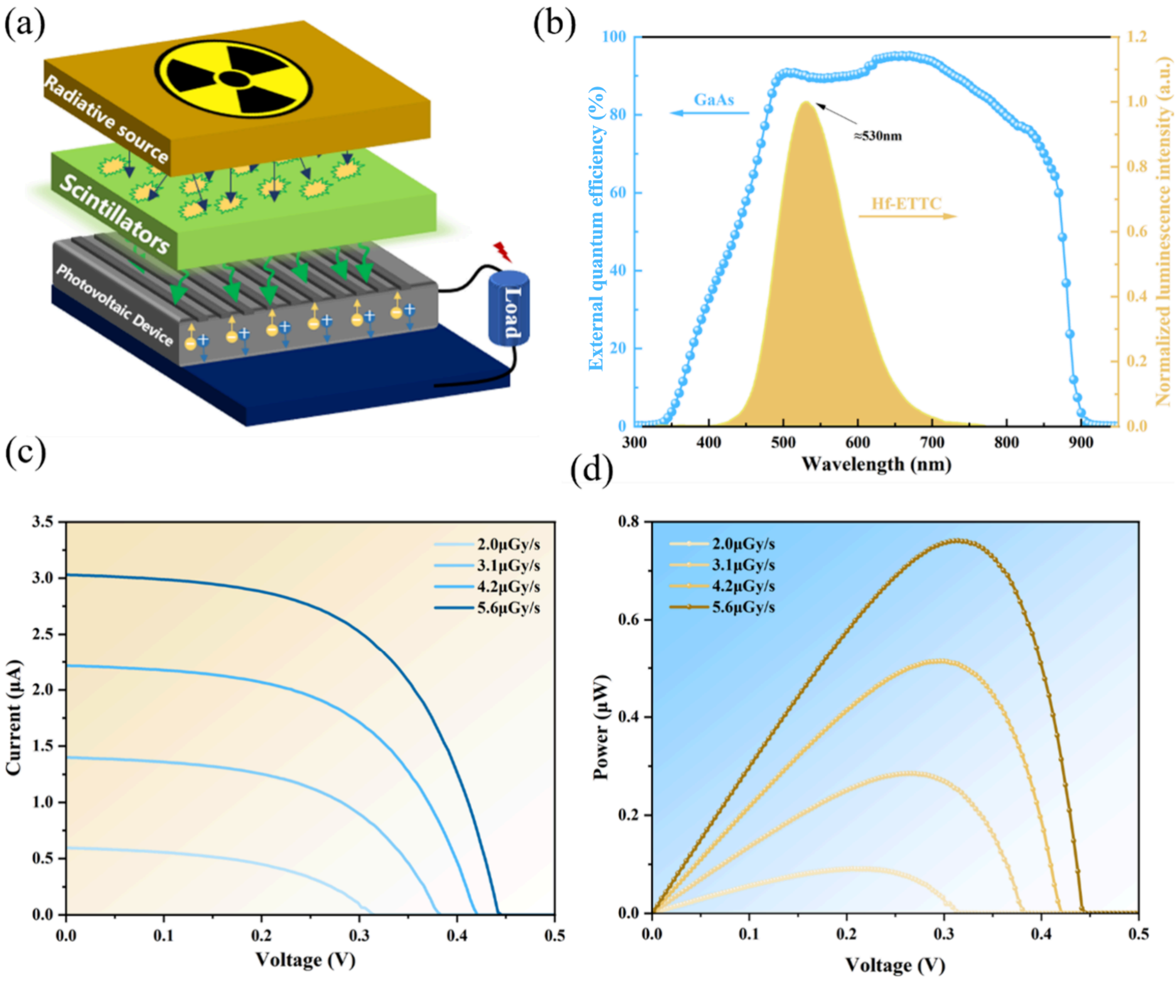

Figure 5. (a) Schematic diagram of the operational mechanism of a radioluminescent nuclear battery. (b) RL spectrum of Hf-ETTC overlaid with the external quantum efficiency (EQE) curve of the GaAs photovoltaic module. (c) Current−voltage ($I-V$) and (d) power−voltage ($P-V$) characteristic curves of the radioluminescent nuclear battery based Hf-ETTC@PDMS composite films.

old dose rate as low as 1.1 μGy s^{-1}, well below the medical diagnostic X-ray dose rate standard of 5.5 μGy s^{-1}.[39] Proof-of-concept imaging experiments were conducted using a capsule containing a spring, ceramic igniter, and pen as test objects (Figure 6d). The internal structures of these items were clearly resolved in the acquired images. Quantitative evaluation of imaging quality via point spread function analysis along the red line across the pen tip in Figure 6d revealed that the Hf-ETTC@PDMS film achieved a spatial resolution with a full width at half-maximum (FWHM) of 402 μm (Figure 6e). This resolution surpasses the previously reported value of 504 μm.[40] Collectively, these results highlight the strong potential of flexible Hf-ETTC@PDMS films for practical X-ray imaging applications, particularly in healthcare diagnostics and security screening.

3. CONCLUSIONS

In this study, a Hf-ETTC incorporating high-Z metal centers and AIE-active ligands achieved a record-high PLQY of 90.72%, nearly double that of the free AIE-active ligand. The synergistic interaction between metal-clusters and ligands endowed the material with exceptional X-ray response characteristics, including a 5-fold enhancement in RL intensity and industry-leading detection sensitivity down to 1.1 μGy s^{-1}. The material also demonstrated excellent environmental stability, retaining 82% of its RL intensity after 60 days of water immersion, and remarkable radiation hardness, maintaining 78% RL output after exposure to 5980 Gy. Using a scalable blade-coating method, we fabricated a flexible Hf-ETTC@PDMS composite scintillating membrane. On this basis, a radioinduced luminescence nuclear battery and an X-ray imaging platform were developed. These results demonstrate the strong potential of Hf-ETTC@PDMS for efficient X-ray energy conversion and advanced imaging applications. Overall, this work establishes a cooperative ″high-Z element/AIE ligand″ design paradigm, offering a versatile material platform for next-generation flexible radiation detection technologies with transformative potential in medical imaging, nuclear monitoring, and self-powered radiation sensing applications.

4. EXPERIMENTAL SECTION

4.1. Materials and Measurements. All reagents were purchased from Macklin Inc. and used without further purification. Powder X-ray diffraction (PXRD) data were collected using a PANalytical Empyrean diffractometer with Cu Kα radiation (λ = 1.54184 Å). Morphological analysis was performed using a TESCAN LYRA3 GM field-emission scanning electron microscope (FE-SEM) operated at an accelerating voltage of 20 kV. Thermogravimetric analysis (TGA) was performed on a Mettler Toledo instrument under a nitrogen atmosphere in the temperature range of 30−800 °C, with a heating

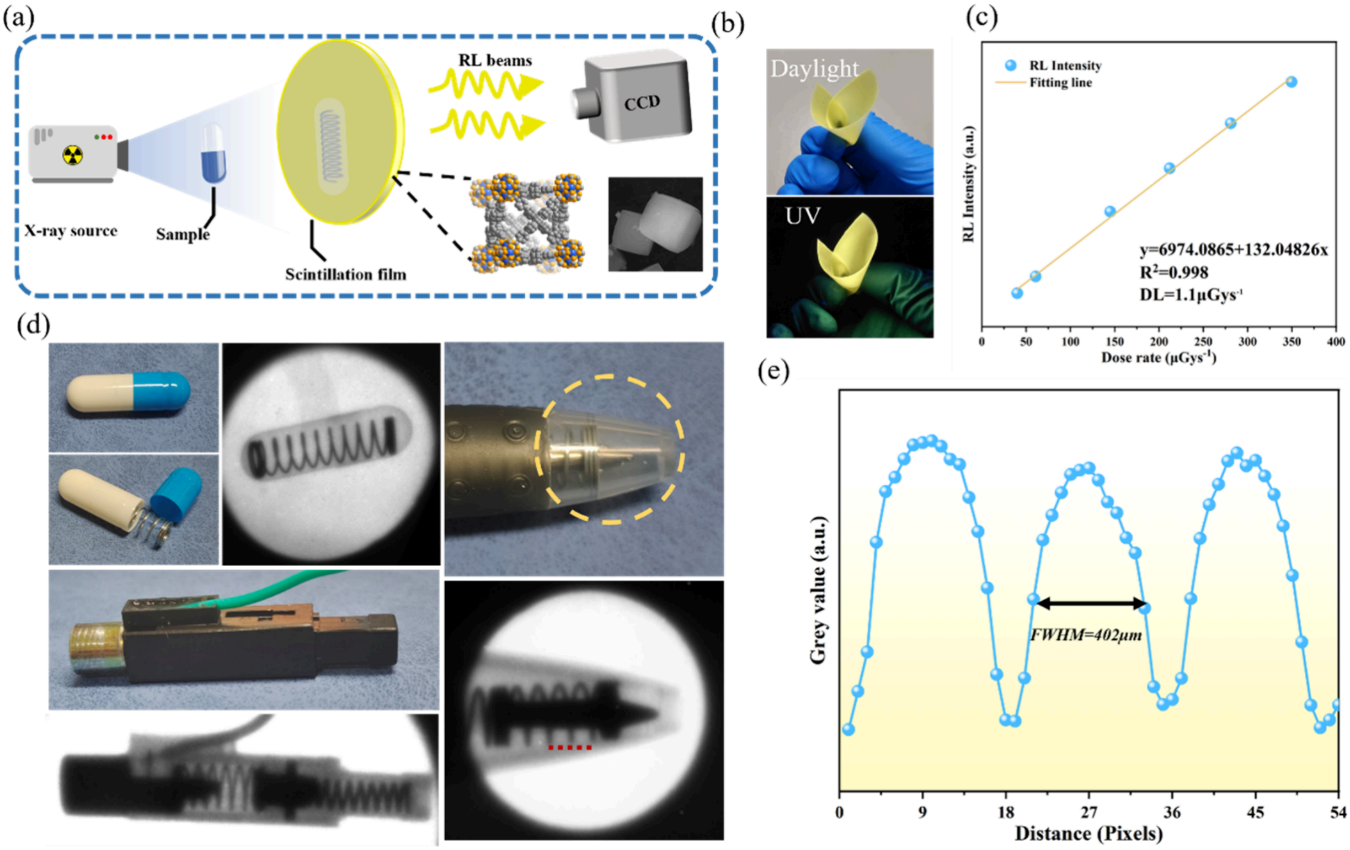

Figure 6. (a) Schematic illustration of the X-ray imaging mechanism using the Hf-ETTC@PDMS flexible scintillation film. (b) Digital photographs of the Hf-ETTC@PDMS film under ambient light and UV illumination (365 nm). (c) Linear correlation between RL intensity at the emission maximum (530 nm) and X-ray dose rate for Hf-ETTC. (d) Photograph of the target material and the corresponding X-ray image. (e) Spatial resolution of X-ray imaging along the red line position of the pen in panel (d).

rate of 10 °C min^{-1}. FTIR spectra was acquired using a Nicolet iS50 FTIR spectrometer.

4.2. Synthesis of Hf-ETTC. In a 50 mL Pyrex reaction vial, hafnium(IV) chloride ($HfCl_4$, 0.865 mmol, 277 mg) and tetracarboxylic ligand H_4ETTC (4′,4‴,4⁗′,4‴‴′-(ethene-1,1,2,2-tetrayl)tetrakis-([1,1′-biphenyl]-4-carboxylic acid), 0.18 mmol, 100 mg) were dissolved in 20 mL of *N*,*N*-dimethylformamide (DMF). Acetic acid (1.3 mL) was then added to the solution. The mixture was ultrasonicated until a clear yellow solution was produced, sealed, and heated at 120 °C for 24 h in a convection oven. Upon cooling to room temperature (~25 °C), yellow crystalline Hf-ETTC precipitated. The product was washed three times each with DMF and ethanol and then collected and dried for further characterization.

4.3. Gas Adsorption Measurements. Prior to analysis, samples were immersed in ethanol for 24 h to remove residual solvent molecules, followed by vacuum activation at 120 °C for 12 h. N_2 adsorption−desorption isotherms were recorded at 77 K using a Micromeritics ASAP 2460 automated surface area and porosity analyzer. The Brunauer−Emmett−Teller (BET) method was used to determine the specific surface area, and the pore size distribution and pore volume were calculated from the adsorption data of the isotherm.

4.4. Characterization of the Photophysical Properties. UV−vis absorption spectra were recorded by using an OPTOSKY UV3610 UV−vis spectrophotometer. PL and RL spectra were obtained by using an Agilent Cary Eclipse fluorescence spectrophotometer. Emission spectra were collected under the following conditions: photomultiplier tube (PMT) operating voltage of 1000 V, scan rate of 200 nm·min^{-1}, and slit width of 5 nm for both excitation and emission during PL analysis. RL measurements were conducted under X-ray excitation with a dose rate of 24.02 μGy·s^{-1}. PLQY measurements were carried out using an integrating sphere module integrated to an Edinburgh Instruments FLS1000 fluorescence spectrometer. Both Hf-ETTC and H_4ETTC samples were excited (λ_{exc}) at 420 nm. Fluorescence lifetime data were acquired using time-correlated single photon counting (TCSPC) and the same FLS1000 system.

4.5. Preparation of the Hf-ETTC@PDMS Composite Membrane. As illustrated in Figure S12, the fabrication process commenced by thoroughly mixing the PDMS prepolymer with its curing agent at a 10:1 mass ratio under vigorous mechanical agitation. Finely ground Hf-ETTC powder was subsequently incorporated into the mixture and continuously stirred until homogeneous dispersion. The final formed slurry was subjected to vacuum degassing for 10 min to eliminate trapped air bubbles and then blade-coated onto flat substrates to form 60 μm-thick wet films. Curing was completed in a vacuum oven at 60 °C for 30 min. This optimized fabrication process ensured uniform filler distribution and strong interfacial bonding between the MOF and the polymer matrix.

4.6. Irradiation Experiments and Application Testing. Long-term irradiation stability tests were conducted at the Irradiation Center of Nanjing University of Aeronautics and Astronautics, simulating cumulative high-dose exposure. The current−voltage (*I*−*V*) characteristics of the radioluminescent nuclear battery were evaluated by using a Keithley 2636A source measurement unit (SMU). X-ray energy response spectra were recorded using a integrated spectrometry system (XR-100SDD). X-ray imaging experiments were performed using an Andor iXon Ultra 888 electron-multiplying CCD (EMCCD) camera, paired with a Canon EF 24−70 mm *f*/2.8L II USM zoom lens. Image acquisition was performed with an integration time of 50 ms.

https://doi.org/10.1021/acsami.5c12872
ACS Appl. Mater. Interfaces 2025, 17, 47553−47561

■ ASSOCIATED CONTENT

Supporting Information

The Supporting Information is available free of charge at https://pubs.acs.org/doi/10.1021/acsami.5c12872.

> SEM images and EDS data of Hf-ETTC; TGA results for Hf-ETTC and H_4ETTC; FTIR curves of Hf-ETTC and H_4ETTC; comparison of PLQY between Hf-ETTC and H_4ETTC; PL spectra at different excitation wavelengths; X-ray absorption coefficients of Hf and Zr metals; variable-temperature PL of Hf-ETTC; RL spectra of Hf-ETTC after water immersion and irradiation; PXRD patterns of Hf-ETTC soaked in water for 0 day and 60 days; flowchart of Hf-ETTC@PDMS fabrication; Hf-ETTC@PDMS pictures bent at different angles; X-ray energy spectrum at a dose rate of 5.6 μGy s^{-1}; film tensile length test table; table of energy conversion efficiencies for various scintillators under comparable conditions (PDF)

■ AUTHOR INFORMATION

Corresponding Authors

Zhiheng Xu − *Department of Nuclear Science and Technology, Nanjing University of Aeronautics and Astronautics, Nanjing 211106, China; Key Laboratory of Advanced Nuclear Technology and Radiation Protection, Ministry of Industry and Information Technology, Nanjing 211106, China;* orcid.org/0000-0002-9229-8558; Email: xuzhiheng@nuaa.edu.cn

Xiaobin Tang − *Department of Nuclear Science and Technology, Nanjing University of Aeronautics and Astronautics, Nanjing 211106, China; Key Laboratory of Advanced Nuclear Technology and Radiation Protection, Ministry of Industry and Information Technology, Nanjing 211106, China;* orcid.org/0000-0003-3308-0468; Email: tangxiaobin@nuaa.edu.cn

Authors

Yong Chen − *Department of Nuclear Science and Technology, Nanjing University of Aeronautics and Astronautics, Nanjing 211106, China*

Tiancheng Xu − *Department of Nuclear Science and Technology, Nanjing University of Aeronautics and Astronautics, Nanjing 211106, China*

Zhiyi Xu − *Department of Nuclear Science and Technology, Nanjing University of Aeronautics and Astronautics, Nanjing 211106, China*

Xuebin Zhang − *Department of Nuclear Science and Technology, Nanjing University of Aeronautics and Astronautics, Nanjing 211106, China*

Yuqiao Wang − *Research Center for Nano Photoelectrochemistry and Devices, School of Chemistry and Chemical Engineering, Southeast University, Nanjing 211189, China;* orcid.org/0000-0001-9281-3911

Complete contact information is available at: https://pubs.acs.org/10.1021/acsami.5c12872

Notes

The authors declare no competing financial interest.

■ ACKNOWLEDGMENTS

We acknowledge the Center for Microscopy and Analysis at Nanjing University of Aeronautics and Astronautics for structural characterization of materials. This work was supported by the National Natural Science Foundation of China (Grant No. 12005101) and the Prospective Layout Project of Nanjing University of Aeronautics and Astronautics (Grant No. ILB240161A24).

■ REFERENCES

(1) Hajagos, T. J.; Liu, C.; Cherepy, N. J.; Pei, Q. High-Z Sensitized Plastic Scintillators: A Review. *Adv. Mater.* **2018**, *30* (27), No. e1706956.

(2) Wibowo, A.; Sheikh, M. A. K.; Diguna, L. J.; Ananda, M. B.; Marsudi, M. A.; Arramel, A.; Zeng, S.; Wong, L. J.; Birowosuto, M. D. Development and Challenges in Perovskite Scintillators for High-Resolution Imaging and Timing Applications. *Commun. Mater.* **2023**, *4* (1), 21.

(3) Chen, Q.; Wu, J.; Ou, X.; Huang, B.; Almutlaq, J.; Zhumekenov, A. A.; Guan, X.; Han, S.; Liang, L.; Yi, Z.; Li, J.; Xie, X.; Wang, Y.; Li, Y.; Fan, D.; Teh, D. B. L.; All, A. H.; Mohammed, O. F.; Bakr, O. M.; Wu, T.; Bettinelli, M.; Yang, H.; Huang, W.; Liu, X. All-Inorganic Perovskite Nanocrystal Scintillators. *Nature* **2018**, *561* (7721), 88−93.

(4) Rong, H.; Xu, X.; Yao, J. Y.; Fan, Q.; Zhang, H.; Xu, H.; Luo, J.; Chen, Q.; Sun, Z. High-Resolution Flexible X-Ray Imaging in a Two-Dimensional Mn^{2+}-Doped Perovskite Scintillator. *ACS Appl. Mater. Interfaces* **2025**, *17* (16), 24137−24145.

(5) Zhou, Y.; Chen, J.; Bakr, O. M.; Mohammed, O. F. Metal Halide Perovskites for X-Ray Imaging Scintillators and Detectors. *ACS Energy Lett.* **2021**, *6* (2), 739−768.

(6) Gandini, M.; Villa, I.; Beretta, M.; Gotti, C.; Imran, M.; Carulli, F.; Fantuzzi, E.; Sassi, M.; Zaffalon, M.; Brofferio, C.; Manna, L.; Beverina, L.; Vedda, A.; Fasoli, M.; Gironi, L.; Brovelli, S. Efficient, Fast and Reabsorption-Free Perovskite Nanocrystal-Based Sensitized Plastic Scintillators. *Nat. Nanotechnol.* **2020**, *15* (6), 462−468.

(7) Shen, J.; Jia, R.; Hu, Y.; Zhu, W.; Yang, K.; Li, M.; Zhao, D.; Shi, J.; Lian, J. Cold-Sintered All-Inorganic Perovskite Bulk Composite Scintillators for Efficient X-Ray Imaging. *ACS Appl. Mater. Interfaces* **2024**, *16* (19), 24703−24711.

(8) Zhang, Z.; Tang, X.; Liu, Y.; Xu, Z.; Ye, H.; Tian, F.; Liu, K.; Yuan, Z.; Chen, W. Application of Liquid Scintillators as Energy Conversion Materials in Nuclear Batteries. *Sens. Actuators Phys.* **2019**, *290*, 162−171.

(9) Yu, D.; Wang, P.; Cao, F.; Gu, Y.; Liu, J.; Han, Z.; Huang, B.; Zou, Y.; Xu, X.; Zeng, H. Two-Dimensional Halide Perovskite as β-Ray Scintillator for Nuclear Radiation Monitoring. *Nat. Commun.* **2020**, *11* (1), 3395.

(10) Furukawa, H.; Cordova, K. E.; O'Keeffe, M.; Yaghi, O. M. The Chemistry and Applications of Metal-Organic Frameworks. *Science* **2013**, *341* (6149), 974.

(11) Varma, R.; Baul, A.; Wadhwa, R.; Gulati, S. Introduction to Metal-Organic Frameworks (MOFs). *Met.-Org. Framew. MOFs Catal.* **2022**, *130*, 3−42.

(12) Wang, P. K.; Wang, W. F.; Li, B. Y.; Xie, M. J.; Bian, H. Y.; Wang, S. H.; Zheng, F. K.; Guo, G. C. Flexible Strontium-Based Metal-Organic Framework Scintillation Screens for High-Resolution X-Ray Imaging. *Inorg. Chem. Front.* **2023**, *10* (19), 5710−5718.

(13) Wang, X.; Wang, X.; Song, J.; Bao, H.; Yuan, M.; Wang, Y.; Kong, L.; Liu, W. Anchoring the AIEgen by Zr Clusters in Metal-Organic Gel for Efficient X-Ray Detection and Imaging. *Chem.* **2024**, *10* (4), 1268−1278.

(14) Planas, N.; Mondloch, J. E.; Tussupbayev, S.; Borycz, J.; Gagliardi, L.; Hupp, J. T.; Farha, O. K.; Cramer, C. J. Defining the Proton Topology of the Zr6-Based Metal-Organic Framework NU-1000. *Am. Chem. Soc.* **2014**, *5* (21), 3716−3723.

(15) Meng, Z.; Chen, F.; Shen, P.; Lei, L.; Xu, H.; Xu, S. Luminescence Intensity-Tunable X-Ray Scintillation Based on Zirconium-Based Metal-Organic Frameworks. *J. Solid State Chem.* **2024**, *329*, No. 124425.

(16) Zhang, L.; Wang, X.; Wang, X.; Wang, X.; Luo, Y.; Tan, C.; Jiang, L.; Wang, Y.; Liu, W. Fabrication of a Large-Area Flexible Scintillating Membrane for High-Resolution X-Ray Imaging Using an AIEgen-Functionalized Metal-Organic Framework. *Inorg. Chem.* **2023**, *62* (16), 6421−6427.

(17) Wang, X.; Shi, H.; Ma, H.; Ye, W.; Song, L.; Zan, J.; Yao, X.; Ou, X.; Yang, G.; Zhao, Z.; Singh, M.; Lin, C.; Wang, H.; Jia, W.; Wang, Q.; Zhi, J.; Dong, C.; Jiang, X.; Tang, Y.; Xie, X.; Yang, Y.; Wang, J.; Chen, Q.; Wang, Y.; Yang, H.; Zhang, G.; An, Z.; Liu, X.; Huang, W. Organic Phosphors with Bright Triplet Excitons for Efficient X-Ray-Excited Luminescence. *Nat. Photonics* **2021**, *15*, 187−192.

(18) Wang, J. X.; Gutierrez-Arzaluz, L.; Wang, X.; He, T.; Zhang, Y.; Eddaoudi, M.; Bakr, O. M.; Mohammed, O. F. Heavy-Atom Engineering of Thermally Activated Delayed Fluorophores for High-Performance X-Ray Imaging Scintillators. *Nat. Photonics* **2022**, *16*, 869−875.

(19) Xu, M.; Liu, J.; Wu, W.; Chen, Y.; Ma, D.; Chen, S.; Jie, W.; Zhu, M.; Xu, Y. Metal-Organic Framework Wafer Enabled Fast Response Radiation Detection with Ultra-Low Dark Current. *Nano Res.* **2024**, *17* (4), 2988−2993.

(20) Wang, C.; Volotskova, O.; Lu, K.; Ahmad, M.; Sun, C.; Xing, L.; Lin, W. Synergistic Assembly of Heavy Metal Clusters and Luminescent Organic Bridging Ligands in Metal-Organic Frameworks for Highly Efficient X-Ray Scintillation. *J. Am. Chem. Soc.* **2014**, *136* (17), 6171−6174.

(21) Yang, D.; Li, L.; Liu, S.; Hu, X.; Zhang, X.; Xu, Z.; Guo, S.; Wang, B.; Tang, X.; Chen, Z.; Li, X.; Xu, Q.; Zeng, H. Heavy Atom-Doped Thermally Activated Delayed Fluorescence Cesium Zirconium Halides for Efficient X-Ray Imaging. *Inorg. Chem. Front.* **2024**, *11*, 6448−6454.

(22) Navarrete-Leon, C.; Doherty, A.; Strimaite, M.; Bear, J. C.; Olivo, A.; Endrizzi, M.; Patrick, P. S. Nanoparticle Contrast Agents for Dark-Field X-Ray Imaging. *Nano Lett.* **2025**, *25* (3), 1036−1042.

(23) Vyas, V. S.; Rathore, R. Preparation of a Tetraphenylethylene-Based Emitter: Synthesis, Structure and Optoelectronic Properties of Tetrakis(Pentaphenylphenyl)Ethylene. *Chem. Commun.* **2010**, *46* (7), 1065−1067.

(24) Du, Y.; Li, F.; Ren, X.; Wu, D.; Ma, H.; Kuang, X.; Li, J.; Feng, R.; Wei, Q. Framework-Induced Electrochemiluminescence Enhancement of an AIEgen-Based MOF Coupled with Heterostructured TiO_2 @Ag NPs as an Efficient Coreaction Accelerator for Sensitive Biosensing. *Anal. Chem.* **2024**, *96* (37), 14926−14934.

(25) Yang, S. Y.; Zhang, L.; Kong, F. C.; Chen, Y.; Li, W. J.; Wang, F.; Liu, C.; He, X.; Xiao, X.; Wang, J.; Sun, J.; Chow, P. C. Y.; Kwok, R. T. K.; Lam, J. W. Y.; Tang, B. Z. Scintillators with aggregation-induced emission. *Chem* **2025**, *11* (5), No. 102534.

(26) Geng, L.; Qiao, Y.; Sun, R.; Guo, L.; Li, Z.-Q.; Ma, Y.; Yu, M.-H.; Chang, Z.; Bu, X.-H. Solution-Processable Metal-Organic Framework Featuring Highly Tunable Dynamic Aggregation States. *Adv. Mater.* **2025**, *37* (4), No. 2415511.

(27) Zhao, Y.; Liang, C.; Mei, Z.; Yang, H.; Wang, B.; Xie, C.; Xu, Y.; Tian, J. Oxygen-Enriched MOF-Hemoglobin X-Ray Nanosensitizer for Enhanced Cancer Radio-Radiodynamic Therapy. *ACS Mater. Lett.* **2023**, *5* (12), 3237−3247.

(28) Wei, Z.; Gu, Z. Y.; Arvapally, R. K.; Chen, Y. P.; McDougald, R. N.; Ivy, J. F.; Yakovenko, A. A.; Feng, D.; Omary, M. A.; Zhou, H. C. Rigidifying Fluorescent Linkers by Metal-Organic Framework Formation for Fluorescence Blue Shift and Quantum Yield Enhancement. *J. Am. Chem. Soc.* **2014**, *136* (23), 8269−8276.

(29) Ni, B.; Sun, W. M.; Kang, J.; Zhang, Y. F. Understanding the Linear and Second-Order Nonlinear Optical Properties of UiO-66-Derived Metal-Organic Frameworks: A Comprehensive DFT Study. *J. Phys. Chem. C* **2020**, *124* (21), 11595−11608.

(30) Dawood, S.; Dorris, A.; Davis, K.; Hammer, N.; Rathnayake, H. Synthesis, Characterization, and Photophysics of Self-Assembled Mn(II)-MOF with Naphthalene Chromophore. *J. Phys. Chem. C* **2021**, *125* (1), 792−802.

(31) Perego, J.; Villa, I.; Pedrini, A.; Padovani, E. C.; Crapanzano, R.; Vedda, A.; Dujardin, C.; Bezuidenhout, C. X.; Bracco, S.; Sozzani, P. E.; Comotti, A.; Gironi, L.; Beretta, M.; Salomoni, M.; Kratochwil, N.; Gundacker, S.; Auffray, E.; Meinardi, F.; Monguzzi, A. Composite Fast Scintillators Based on High-Z Fluorescent Metal-Organic Framework Nanocrystals. *Nat. Photonics* **2021**, *15* (5), 393−400.

(32) Tang, W.; Zhang, Z. Realization of Color Tuning via Solid-Solution and Energy Transfer in Ca3xSrx(PO4)2:Eu2+, Mn2+ Phosphors. *J. Mater. Chem. C* **2015**, *3* (20), 5339−5346.

(33) Cooper, L.; Guillou, N.; Martineau, C.; Elkaim, E.; Taulelle, F.; Serre, C.; Devic, T. Zr IV Coordination Polymers Based on a Naturally Occurring Phenolic Derivative. *Eur. J. Inorg. Chem.* **2014**, *2014* (36), 6281−6289.

(34) Liang, D.; Xu, Z.; Yang, D.; Xu, Z.; Yin, W.; Tang, X. Ultra-Stable $CsPbBr_3$-Embedded Polymer Films for Spectrally Tunable X-Ray Nuclear Batteries and Flexible Radiation Imaging Applications. *J. Mater. Chem. C* **2024**, *12* (42), 17115−17121.

(35) He, Y.; Xu, Z.; Wang, H.; Bian, M.; Liu, Y.; Tang, X. Enhanced Radioluminescence and Improved Radioluminescent Nuclear Battery Output Performance More than 50% with SiO_2 Nanosphere Coating. *J. Lumin.* **2023**, *255*, No. 119600.

(36) Lee, H.; Nam, H.; Yeo, H. J.; Yang, H.; Kim, T. High Efficiency over 15% by Breaking the Theoretical Efficiency Limit of Fluorescent Organic Light-Emitting Diodes with Localized Surface Plasmon Resonance Effects. *ACS Appl. Mater. Interfaces* **2023**, *15* (29), 35290−35301.

(37) Schott, R. J.; Weaver, C. L.; Prelas, M. A.; Oh, K.; Rothenberger, J. B.; Tompson, R. V.; Wisniewski, D. A. Photon Intermediate Direct Energy Conversion Using a 90Sr Beta Source. *Nucl. Technol.* **2013**, *181* (2), 349−353.

(38) Xu, Z.; Tang, X.; Liu, Y.; Zhang, Z.; Chen, W.; Liu, K.; Yuan, Z. $CsPbBr_3$ Quantum Dot Films with High Luminescence Efficiency and Irradiation Stability for Radioluminescent Nuclear Battery Application. *ACS Appl. Mater. Interfaces* **2019**, *11* (15), 14191−14199.

(39) Wang, B.; Ouyang, X.; He, X.; Deng, Z.; Zhou, Y.; Li, P. High-Resolution X-Ray Imaging of Mn Enhanced Lead-Free Halide Scintillators in Pixelated Array Structures. *Adv. Opt. Mater.* **2023**, *11* (17), No. 2300388.

(40) Wu, Y.; Chen, J.; Zheng, D.; Xia, X.; Yang, S.; Yang, Y.; Chen, J.; Pullerits, T.; Han, K.; Yang, B. Organo-Metal Halide Scintillator with Weak Thermal Quenching Up to 200 °C. *J. Phys. Chem. Lett.* **2022**, *13* (25), 5794−5800.